THE JOURNAL OF PHYSICAL CHEMISTRY C
A JOURNAL OF THE AMERICAN CHEMICAL SOCIETY

pubs.acs.org/JPCC

Article

Prediction of Ground State Structures and Robust Weyl Fermionic States in MnRhP

Jaspreet Singh, Anuroopa Behatha, Saba Kharabadze, A. N. Kolmogorov, G. Vaitheeswaran,* and V. Kanchana*

Cite This: J. Phys. Chem. C 2022, 126, 17328−17337

Read Online

ACCESS | Metrics & More | Article Recommendations | Supporting Information

ABSTRACT: Topological metals are a new class of materials that feature Fermionic quasiparticles with the presence of non-trivial band crossings near the Fermi level. In this work, we focus on establishing crystal structure ground states and the corresponding topological properties of MnRhP. Under ambient pressure and low temperatures, we find that an orthorhombic oP12 polymorph is favored over the known hexagonal hP9 phase. Pressures above 15 GPa stabilize tetragonal (tP6′), hexagonal (hP9′), and orthorhombic (oP12′) phases with inverted population of metal sites. While oP12′ has the lowest enthalpy, we show that hP9′ is more consistent with the previous X-ray diffraction data collected at 60 GPa. Our analysis of hP9 and oP12 topological properties reveals the existence of nodal lines around the Γ-point that are gapped out when spin−orbit coupling effects are included and transform into Weyl nodes with opposite chirality near the Fermi level. The calculated large values of the anomalous Hall conductivity in hP9, oP12, and tP6′ and the Z_2 topological invariant in the non-magnetic hP9′ can be used to verify the predicted non-trivial robust topological features of MnRhP under ambient and high pressures.

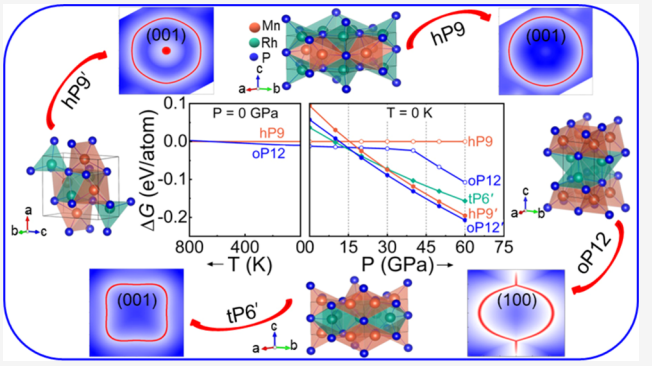

INTRODUCTION

Developing experimental tools for synthesis and study of material properties under extreme conditions has dramatically expanded the range of attainable chemical compositions and crystal structures in material research.[1−4] Diamond-anvil cells and large-volume presses like multi-anvil or piston-cylinder devices generate the static pressures, whereas large-scale shock-wave facilities generate dynamic compression. In addition to these experimental techniques, there has been notable progress in developing theoretical methods that guide experimentalists.[5−10] The combination of crystal structure prediction and first-principles analysis can identify synthesizable materials with appealing properties.[2,11−15]

Topological metals (TMs)/semimetals have attracted tremendous attention because they display a multitude of exotic features.[16−20] TMs host the linearly dispersive electrons, which can be described by Dirac/Weyl relativistic equation. The classification of TMs includes nodal points[20−22] and nodal lines (NLs)/rings,[20,23,24] and they have a straightforward relevance with the type of band crossing or band touching points in the electronic band structure. These band crossings form a closed loop inside the Brillouin zone (BZ) in NL semimetals protected by certain symmetries, such as time-reversal, mirror reflection, or spin-rotation symmetries. The NL could be either fully gapped or gapped into several nodal points by including the spin−orbit coupling (SOC).[25−27] For instance, Fe_2P-type compounds, such as ZrRuP,[28] HfRuP,[29] CaAgP, and CaAgAs,[30] are of interest for their electronic properties with an NL.

Our present work focuses on the transition-metal ternary pnictide MnRhP, which belongs to the family of Fe_2P-type MnMX intermetallic compounds, well known for their interesting magnetic and structural properties at ambient and elevated pressures. In general, the transition-metal ternary pnictides, MM′X [M = 3d transition metal, M′ = 4d transition metal, and X = metalloid atom (P, As or Sb)], crystallize in the hexagonal Fe_2P-type, orthorhombic Co_2P-type, or tetragonal Cu_2Sb-type structure[31] with different magnetic behaviors. In the past years, Kanomata et al.,[32] Ohta et al.,[33] and Harada et al.[34] investigated the magnetic and electronic properties of several MM′X compounds. The Mn-based compounds, MnMX (M = Ru, Rh, Pd and X = P, As), crystallize in the hexagonal Fe_2P-type, each featuring tetragonal (with 4d atoms) and square-base

Received: June 30, 2022
Revised: September 12, 2022
Published: September 29, 2022

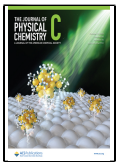

https://doi.org/10.1021/acs.jpcc.2c04603
J. Phys. Chem. C 2022, 126, 17328−17337

pyramidal (with 3d atoms) metal sites with pseudo two-dimensionality along the *c*-axis.[32]

Many essential features of solid-state materials have been discovered, including phase transitions, which are caused by changes in either pressure or temperature or both. As an example, the Fe_2P compound undergoes a magnetic phase transition above 5 kbar.[35] According to Fujii et al., MnRhAs undergo a magnetic phase transition from an antiferromagnetic (AFM) state to a ferromagnetic (FM) state at 5 GPa.[36] From the X-ray diffraction (XRD) measurements of MnRhAs, a structural phase transition from a hexagonal phase to an orthorhombic one was found at 26 GPa.[37] Similarly, the AFM hexagonal MnRuP transforms into a hexagonal/orthorhombic multi-phase mixture and is found to be FM in nature.[38] Pressure plays an important role in modifying the Curie temperature (T_C) as well. In the case of MnRuAs and MnPdAs, the Curie temperature was found to decrease with applied pressure (up to 1.1 GPa), whereas MnRhP exhibits a different behavior. The value of T_C increases linearly with a pressure up to 1.1 GPa. MnRhAs show behavior similar to that of MnRhP. The reported values of dT_C/dP for MnRhP and MnRhAs are +11.6 and +7.1 K/GPa, respectively.[39,40]

MnRhP has been investigated at ambient and high pressures and shown to exhibit an FM behavior with a T_C of 400 K.[32] The magnetic moment of MnRhP at 4.2 K was found to be 3.0 μ_B per formula unit. The spontaneous magnetization of MnRhP at a low temperature (4.2 K) was investigated up to 0.76 GPa, and it was observed that the T_C of MnRhP increases linearly with pressure, and the value of dT_C/dP is +1.2−1.5 K/kbar.[41,42] Diamond-anvil cell experiments and powder XRD measurements have also revealed a pressure-induced phase transition from the hexagonal to an orthorhombic crystal structure at 34 GPa, but the collected data was insufficient to determine the space group of the new phase(s).[37] Considering a common emergence of topological states accompanying high-pressure magneto-structural transitions in Fe_2P-type compounds, one can expect MnRhP to exhibit interesting physics under certain (P, T) conditions as well.

In this study, we have performed a systematic characterization of the MnRhP compound's structural, electronic, magnetic, and topological properties. We began by carrying out evolutionary searches to establish ground state structures in a range of pressures and temperatures. Our thermodynamic stability analysis at ambient pressure indicates that an orthorhombic oP12 phase has lower energy compared to the experimentally observed hP9 polymorph and could be the low-temperature ground state. At high pressures, we identified three competing phases with an inverted population of metal sites, tP6′, hP9′, and oP12′, that become more stable than the hP9/oP12 counterparts around 15 GPa. Our electronic band structure analysis reveals non-trivial topological properties of these ambient and high-pressure phases. When SOC is ignored, all phases possess NLs near the Fermi energy. With the inclusion of SOC, the NLs turn into the pairs of Weyl points in the hP9, oP12, tP6′ (due to the lack of the time-reversal symmetry), and hP9′ (due to the absence of the inversion symmetry) phases. In addition, the hP9′ phase shows a non-trivial topological nature with Z_2 indices. Our results suggest that MnRhP does host a wealth of intriguing properties and warrants further experimental study.

Theoretical Methods. We used the Vienna ab initio simulation package (VASP)[43−45] to perform first-principles calculations in the framework of density functional theory (DFT). The Perdue−Burke−Ernzerhof (PBE) exchange−correlation functional within the generalized gradient approximation (PBE−GGA)[46] was chosen as the default method, but the stability of selected structures was also checked with the local density approximation (LDA),[47,48] optB86b,[49] and strongly constrained and appropriately normed (SCAN)[50] functionals. The projector augmented wave (PAW) potentials with valence configurations $3p^64s^23d^5$, $4p^65s^14d^8$, and $3s^23p^3$ were adopted for "Mn," "Rh," and "P," respectively.[45] We performed all final static calculations with the energy cutoff and the energy convergence criteria of 500 and 10^{-6} eV, respectively, to ensure good numerical convergence of the relative energies and forces with respect to the plane-wave basis. Dence Monkhorst-Pack[51] k-point meshes have been used to achieve numerical convergence to within 1−2 meV/atom. Global searches for high-pressure ground states were driven by an evolutionary algorithm implemented in module for ab initio structure evolution (MAISE).[10] Populations of 16−20 structures with 2−4 MnRhP formula units were generated randomly and evolved with standard mutation and crossover operations[10] for 20−50 generations. The spin-polarized-relativistic Korringa−Kohn−Rostoker method SPRKKR[52] was used to determine the magnetic interaction between "Mn" atoms, which provides the Heisenberg exchange coupling constants (J_{ij}). The density functional perturbation theory using VASP with the combination of PHONOPY has been used to determine the phonon properties.[53] As a next step, we have constructed a tight-binding Hamiltonian H, using WANNIER90 and WANNIERTOOLS packages, to determine the topological properties such as surface states, Berry curvature, and anomalous Hall conductivity (AHC).[54,55]

RESULTS AND DISCUSSION

Ground State Structure Search and Pressure-Induced Phase Transitions. *Identification of Ground State Candidates.* Intermetallic MM′X compounds have been observed in hexagonal Fe_2P (hP9), orthorhombic Co_2P (oP12), or tetragonal Cu_2Sn (tP6) prototypes, each featuring tetragonal, $M^{(4)}$, and square-base pyramidal, $M^{(5)}$, metal sites (Figure 1a). Our evolutionary search for 9-atom unit cells at 40 GPa converged to a hP9′ phase (Figure 1b), a significantly more stable variant of the ambient-pressure hP9-$Mn^{(5)}Rh^{(4)}P$ prototype with the inverted population of the "Mn" and "Rh" sites. The finding prompted us to examine tP6′ and oP12′ polymorphs with swapped metal sites as well. For the orthorhombic prototype, the $Mn^{(4)}Rh^{(5)}$ configuration was found to become more stable than $Mn^{(5)}Rh^{(4)}$ above 15 GPa, while for the tetragonal prototype, $Mn^{(4)}Rh^{(5)}$ proved to be favored over $Mn^{(5)}Rh^{(4)}$ at all pressures. Further 6-, 9-, and 12-atom evolutionary searches at 40 and 50 GPa produced no other potential ground state candidates.

Analysis of Structure Stability. The following tests help illustrate the importance of metal coordination in the thermodynamic stability of MnMP compounds. Figure 2a shows the significance of the magnetic ordering in the stability of phases with the $Mn^{(5)}Rh^{(4)}$ and $Mn^{(4)}Rh^{(5)}$ populations of metal sites as a function of pressure. Under ambient conditions, the magnetic energy is a substantial stabilizing factor for the phases with the "Mn" atoms on the pyramidal sites, while it is either small (oP12′ and tP6′) or non-existent (hP9′) when the "Mn" atoms are on the tetragonal sites. Unsurprisingly, compression reduces the magnetic contribution in all cases, completely suppressing it in oP12 and oP12′ by 40 GPa (the resulting reduction of the effective "Mn" size in the low-spin state causes a change in relative enthalpy slope in Figure 1b). Figure 2b

https://doi.org/10.1021/acs.jpcc.2c04603
J. Phys. Chem. C 2022, 126, 17328−17337

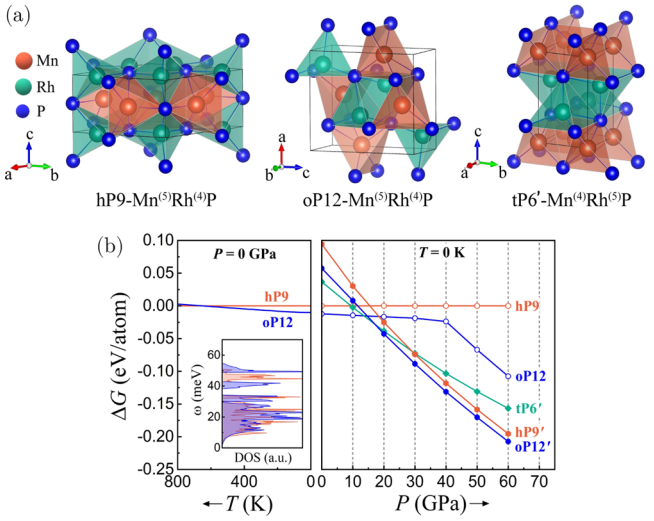

Figure 1. (a) Competing structures for MnRhP. "Mn," "Rh," and "P" atoms are shown in orange, green, and blue, respectively. The superscript shows the coordination of the metal site. The observed ambient-pressure phase is hP9-$Mn^{(5)}Rh^{(4)}P$, while hP9′-$Mn^{(4)}Rh^{(5)}P$, oP12′-$Mn^{(4)}Rh^{(5)}P$, and tP6′-$Mn^{(4)}Rh^{(5)}P$ become more stable under compression. (b) Relative Gibbs free energy of the MnRhP phases with respect to hP9 as a function of temperature (left) and pressure (right) obtained with spin-polarized calculations. The Pearson symbols with primes denote phases with $Mn^{(4)}Rh^{(5)}$ rather than the traditional $Mn^{(5)}Rh^{(4)}$ metal site occupation. Note that tP6 is unstable at all pressures by at least 0.13 eV/atom compared to hP9, while tP6′ may be thermodynamically stable in a narrow pressure range around 15 GPa. The inset shows phonon density of states (DOS) for the two competing phases at ambient pressure.

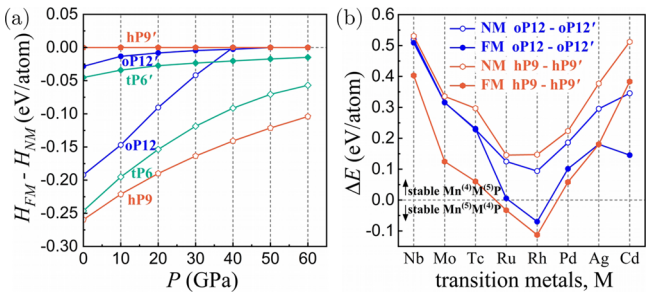

Figure 2. (a) Enthalpy difference between FM and non-magnetic (NM) configurations in MnRhP phases as a function of pressure. The primed labels denote phases with the inverted population of metal sites ($Mn^{(4)}Rh^{(5)}P$). (b) Energy difference in hexagonal and orthorhombic structures with a direct and inverted population of metal sites for different transition metals "M". The solid and hollow points show FM and NM values.

illustrates the interplay between the magnetic stabilization and the chemical pressure for a series of MnMP compounds with 4d transition metals. That is, the $Mn^{(5)}M^{(4)}$ arrangement causes a considerable energy penalty, at least 0.1 eV/atom, because the transition metal ions are noticeably larger than the "Mn" ions and prefer to be on the larger pyramidal sites. However, this metal decoration allows for substantial magnetic energy gains, up to 0.25 eV/atom, due to the FM ordering arising on $Mn^{(5)}$ sites. As a result, $Mn^{(5)}M^{(4)}P$ proves favorable over $Mn^{(4)}M^{(5)}P$ for the "Ru" and "Rh" transition metals that have the smallest effective sizes in the series.

Calculation of Thermodynamic Corrections. Our calculations at ambient pressure and zero temperature indicate that oP12 is lower in energy than the hP9 phase observed experimentally. A similar outcome was reported for the binary Fe_2P compound by Bhat et al.,[56] who demonstrated that the inclusion of vibrational entropy corrections makes hP9 the ground state above 300 K. They estimated that the zero-point spin fluctuation term further stabilizes hP9-Fe_2P by 23.6 meV/atom and suggested that the hexagonal phase could be stable at all temperatures. We reproduced the phonon results for Fe_2P, obtaining similar energy differences and transition temperature values for the oP12 and hP9 polymorphs (Figure S1a). In MnRhP, the vibrational entropy is found to stabilize hP9 as well, albeit at higher temperatures above ∼650 K (Figure 1b). The free energy contributions arising from spin fluctuations are difficult to evaluate accurately due to the number of approximations involved.[56] However, one can expect their effect on the MnRhP polymorphs' relative stability to be small due to the closeness of the calculated magnetic moments of 3.12 μ_B/f.u. in hP9 and 3.15 μ_B/f.u. in oP12, in contrast to the markedly different calculated values of 2.96 μ_B/f.u. in hP9 and 1.77 μ_B/f.u. in oP12 for Fe_2P. Moreover, the importance of spin fluctuations in a particular material can be deduced from an appreciable suppression of the total magnetic moment by comparing values measured experimentally and calculated within the mean-field framework of DFT.[57] Considering that the experimental magnetic moments of 3.0 μ_B/f.u. in hP9-MnRhP[41,42] and 3.0 μ_B/f.u. in hP9-Fe_2P[58] agree well with the corresponding DFT values, spin fluctuations in this hexagonal structure appear to be insignificant. We conclude that oP12-MnRhP could be a true ambient-pressure ground state at low temperatures.

Reliability of the DFT-Based Ground State Determination. In order to check the sensitivity of these results to the DFT systematic errors, we calculated the relative energy with different functionals and found oP12 to be consistently favored over hP9: by −12.2 meV/atom (GGA-PBE), −12.0 meV/atom (optB86-b), −21.3 meV/atom (LDA), and −13.4 meV/atom (SCAN). Inclusion of SOC changed the PBE-GGE value by an insignificant 0.5 meV/atom. Disagreements between DFT ground state predictions and experimental observations are not uncommon and can also arise from the reaction kinetics. For example, our recent DFT analysis of Cu_3Sn showed that the most commonly observed 10-fold superstructure is metastable relative to a much simpler prototype that had been reported only once,[59] while new high-pressure or high-temperature phases of LiB, FeB_4, and $NaSn_2$ predicted with similar methods in our previous studies have been later synthesized and successfully annealed down to ambient conditions.[10]

Interpretation of the Reported High-Pressure Experimental Phase. Figure 1b demonstrates that the orthorhombic phase (oP12′) is favored over the hexagonal analog (hP9′) at high pressures as well. However, the simulated XRD pattern for the oP12′ phase with 4 formula units does not match the previously reported experimental XRD data[37] that was interpreted as an orthorhombic cell with 6 formula units (Figure 3). In fact, the reported lattice parameters a = 5.945 Å, b = 10.453 Å, and c = 3.185 Å at 60 GPa correspond closely to those in the orthorhombic representation of the hexagonal hP9 structure (a = 5.889 Å, $b = \sqrt{3}a$ = 10.200 Å, and c = 3.268 Å). Nevertheless, neither the fully optimized hP9 nor its orthorhombic representation constrained to the experimental lattice constants has XRD reflections matching well the collected data at 60 GPa (Figure S2a). On the other hand, Figure 3 reveals a similar level of agreement between the experiment and our

https://doi.org/10.1021/acs.jpcc.2c04603
J. Phys. Chem. C 2022, 126, 17328−17337

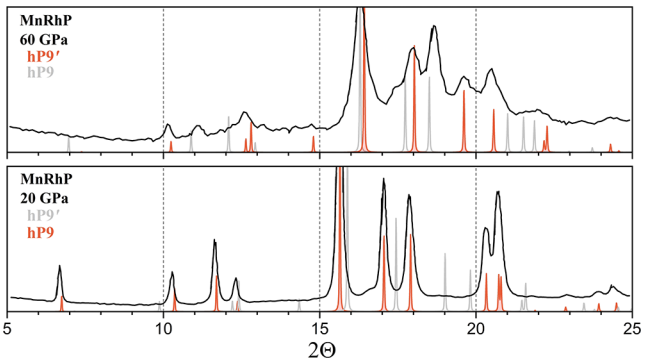

Figure 3. Comparison of experimental XRD patterns reported in ref 37 and our simulated XRD patterns (orange and gray) for MnRhP under high pressures. At 20 GPa, the experimental observation agrees well with the known ambient-pressure hP9 phase. At 60 GPa, the experimental pattern is consistent with the hP9′ phase as explained in the text. The simulated patterns for hP9 and hP9′ are shown at each pressure to illustrate that the two closely related phases have considerably different XRD features.

simulations if we use hP9 at 20 GPa and hP9′ at 60 GPa, as the main peaks are shifted by 1−2% typical for the DFT systematic errors. The only notable discrepancy in the latter case is the presence of two prominent peaks around 11.0 and 18.5° in the experimental data. Dynamic instability of the hP9′ phase at 60 GPa could explain the orthorhombic distortion, but our phonon calculations revealed no imaginary modes (Figure S1c) and the lattice constants a = 5.559 Å, $b = \sqrt{3}\,a$ = 9.629 Å, and c = 3.473 Å and the atomic volume at 60 GPa (Figure S1d) are not close to those extracted from the experimental data. Moreover, simulated 2% orthorhombic distortions of hP9′ in Figure S2b split the XRD peaks defined by the h and k indices by about 1° but do not generate new visible reflections around 11.0 and 18.5°. Another possibility is the presence of multiple phases in the sample, a common occurrence in high-pressure experiments that complicates the interpretation of XRD data.[4,15] Finally, non-hydrostatic compression or kinetics-driven transformation may leave the material trapped in a metastable state.[15,60−63] These factors are particularly relevant in the present case because the standard 4:1 methanol−ethanol mixture used as pressure medium by Eto et al.[37] ensures hydrostatic conditions only up to about 10 GPa.[64,65] Room-temperature non-hydrostatic compression not only makes it difficult to obtain well-resolved XRD reflections but also renders the lowest Gibbs free energy to not be a definitive criterion for selecting candidate structures. According to our simulations, neither the previously proposed nor the presently considered orthorhombic derivatives of the hexagonal structures appear to explain the observed XRD patterns. The identified metastable hP9′ polymorph that offers a better match of major peak positions and intensities may be helpful for establishing MnRhP high-pressure phase(s) in future studies.

Structural Properties. The hP9 phase of intermetallic compound MnRhP is a symmorphic phase with space group $P\bar{6}2m$ (189) that does not possess inversion symmetry. The space group has a threefold rotational axis (C_{3z}) and a horizontal mirror plane (m_{001}). The lattice constants (a = 6.244 Å and c = 3.575 Å) and the atomic volume (V = 120.71 Å^3) of the unit cell optimized in our DFT calculations are in good agreement with the corresponding experimental values at ambient pressure (a = 6.223 Å, c = 3.585 Å, and V = 120.23 Å^3).[37] "Mn" and "Rh" are positioned at the pyramidal (3g) and tetrahedral (3f) sites, respectively. From Figure 4a, it can be seen that Mn + P and Rh + P atoms form layers that are separated along the c-axis. The bulk and (001) projected surface BZs are shown in Figure 4b.

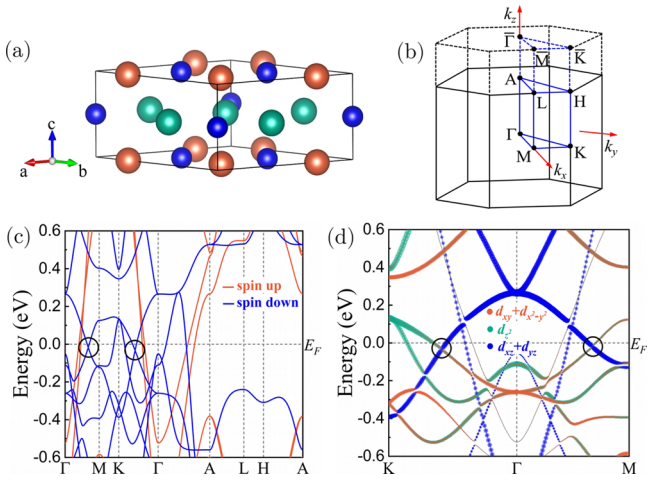

Figure 4. (a) Crystal structure of MnRhP with hexagonal (hP9) symmetry. (b) Irreducible BZ of the bulk along with the (001) projected surface. (c) Electronic band structure of MnRhP along with high symmetry path. (d) Electronic band structure with SOC along the [100] direction.

We have also analyzed the identified orthorhombic phase (oP12) with the space group *Pnma* (62). There are four formula units in the primitive unit cell of oP12, where all atoms are positioned at 4c as shown in Figure 5a. Similar to hP9, "Mn" and

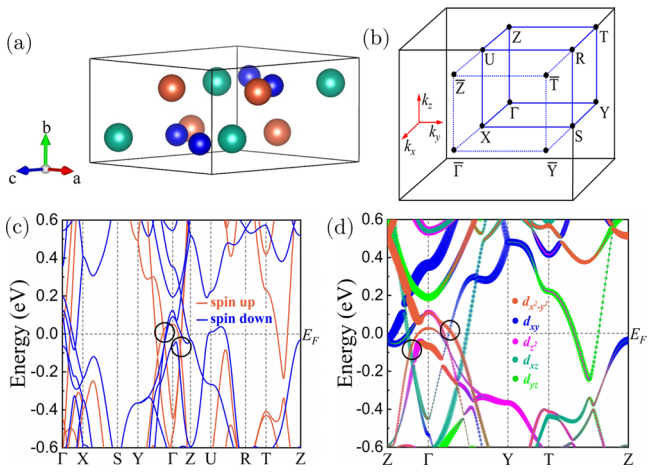

Figure 5. (a) Crystal structure of MnRhP with orthorhombic (oP12) symmetry. (b) Irreducible BZ of the bulk along with the (100) projected surface. (c) Electronic band structure of MnRhP along with high symmetry path. (d) Electronic band structure with SOC along the [100] direction.

"Rh" atoms are located at the pyramidal and tetrahedral sites, respectively, in the oP12 structure. The nonsymmorphic space group *Pnma* contains three screw-axis symmetries (S_{2x}, S_{2y}, and S_{2z}) and three glide-plane symmetries (G_x, G_y, and G_z). In contrast to hP9, oP12 possesses the inversion symmetry. Apart from that, to check the dynamic stability of all phases, we have calculated the dynamic properties, which have been given in the Supporting Information.

https://doi.org/10.1021/acs.jpcc.2c04603
J. Phys. Chem. C 2022, 126, 17328−17337

Magnetic and Electronic Properties. To get more insights into the magnetic ground state of the system, we have computed different magnetic orderings (FM and AFM) in both the ambient phases, that is, hP9 and oP12 phases (see Supporting Information for more information). FM turns out to be the energetically most stable in both phases. Our results report the total magnetic moment to be 3.12 μ_B (3.15 μ_B) per f.u. for the hP9 (oP12) phase, which agrees well with the experimental observations.[41,42]

Figure 4c highlights the band structure of hP9−MnRhP with the spin-up channel in orange and a spin-down channel in blue color along with the high-symmetry points Γ-M-K-Γ-A-L-H-A. We plotted the partial DOS (PDOS) as shown in Figure S5c to examine the atomic orbital contributions near the Fermi level. It can be seen in the PDOS (Figure S5c) that the MnRhP has a metallic appearance and that the Mn-d and Rh-d states contribute at the Fermi level. A large energy gap of about 3.5 eV separated the DOS into two manifolds with the core valence states of predominantly P-3*s* character ranging from −14 to −11 eV.

We discovered several band-touching points near the Fermi level along the Γ-M-K-Γ path (i.e., in the $k_z = 0$ plane) from the spin-down channel, as shown in Figure 4c. These crossing points suggest that the system contains a topological NL protected by a mirror symmetry in the *xy*-plane. As the system lacks space inversion symmetry, switching on the SOC lifts the band degeneracy and exhibits band inversion in the spin-down channel around the Γ-M and K-Γ paths between $d_{x^2-y^2} + d_{xy}$ and $d_{xz} + d_{yz}$ of the "Mn" atom (Figure 4d). This leads to a gapless NL centered at the Γ-point in the horizontal $k_z = 0$ plane, which is similar to the corresponding features in TaS.[66]

In order to confirm the topological features, we have done the surface state calculations for the (001) plane using the WANNIER package. Figure 6a gives details of the (001) projected surface state, which highlights the NL dispersion from the bulk bands and the emergent drumhead surface states (DSS), along with the gap plane at the chemical potential

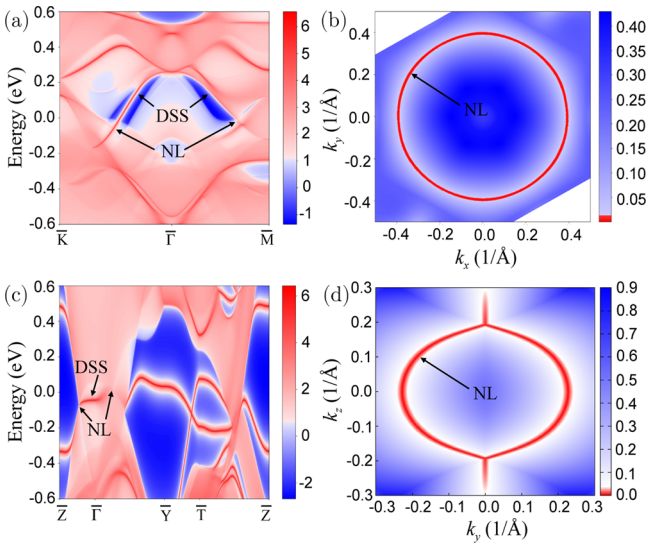

Figure 6. (a) Calculated (001) surface projected band structure of MnRhP in its hP9 phase, highlighting the NL and the existence of drumhead-like surface states. (b) Corresponding gap plane showcases the system's NL. (c) (100) projected surface states of the oP12 phase with (d) energy gap plane, which show the NL in this phase.

corresponding to the NL (Figure 6b). The above-mentioned results confirm that MnRhP in its observed ambient-pressure hP9 phase hosts the NL.

Next, we have analyzed the ambient oP12 phase of MnRhP and provided the details in Figure 5. In order to examine the atomic orbital contributions close to the Fermi level, we have plotted PDOS (Figure S5d), which reflects the metallic behavior of our compound in both spin channels contributed by d states of "Mn" and "Rh" atoms.

Remarkably, we spotted some interesting crossing points around the Γ-point close to the Fermi level along the high-symmetry Y-Γ and Γ-Z paths (i.e., in $k_x = 0$ plane) from the spin-up channel (Figure 5c). The existence of band inversion along the Y-Γ path with $d_{x^2-y^2} - d_{xy}$ and along the Γ-Z path with $d_{x^2-y^2} - d_{xz}$ of the "Mn" atoms is responsible for the Γ-centered NL as shown in Figure 5d. This NL is protected by symmetry operation G_x.

The band dispersions projected onto the (100) surface are shown in Figure 6c. Topological surface states are clearly evident on the projected (100) surface, linking the two gapless points within $\bar{\Gamma}$-$\bar{Y}$ and $\bar{\Gamma}$-$\bar{Z}$ and generating a two-dimensional DSS, a signature of a topological NL semimetal. The gap plane calculation further confirms the presence of an NL in our system, as shown in Figure 6d.

We have also included the SOC in the system to estimate the magnetocrystalline anisotropic energy (MAE) and found that the [100] magnetization direction (i.e., spins aligning in the *x*-direction) is the easy axis and MAE is about 0.1 and 0.7 meV/atom in the hP9 and oP12 phase, respectively. The details of total and on-site magnetic moments of MnRhP and constituent atoms in both phases are given in Table 1, which confirms that the total magnetic moment is mainly because of the transition element, "Mn".

However, the crystal symmetries depend upon the magnetization direction. In the case of the hP9 phase, the inclusion of SOC along the [100] direction breaks the horizontal mirror plane m_{001} and splits out the Γ-centered NL. With SOC, the system preserves rotational symmetry C_{2x}, and it may possess Weyl points, which can be determined by searching the whole BZ. We found that the hP9 phase exhibits six pairs of Weyl nodes with opposite chirality as shown in Table 2. Similarly, magnetization along the [100] direction in the oP12 phase breaks the screw-axis rotation (S_{2y} and S_{2z}) and glide mirror symmetries (G_y and G_z) while preserving the inversion, glide mirror G_x, and screw-axis rotation symmetry S_{2x}. The symmetry breaking allows the gapped NL and transition into hidden Weyl points. In this case, we obtained two pairs of Weyl nodes, which are given in Table 3. Weyl points for both phases are marked in the BZ, and the band dispersions near these Weyl nodes are shown in Figure 7.

Finally, we have examined the electronic properties of MnRhP at 15 GPa in tP6′ ($P4/nmm$) and at 30 GPa in hP9′ ($P\bar{6}2m$) phase. According to the space group of both phases, tP6′ is nonsymmorphic and possesses inversion symmetry, and hP9′ is symmorphic and breaks inversion symmetry. The details of the electronic band structures for both phases are given in Figure S6. In the case of the tP6′ phase, the band-crossing points protected by the glide mirror symmetry (G_z) are found to be close to the Fermi level along the Γ-X-M-Γ path in both spin-up and spin-down channels as shown in Figure S6a. To analyze these crossing points, we have plotted the orbital projected bands with the inclusion of SOC (Figure S6b) and found that there is a band inversion in the spin-up channel around the Γ-X and M-Γ points

https://doi.org/10.1021/acs.jpcc.2c04603
J. Phys. Chem. C 2022, 126, 17328−17337

Table 1. Total and Atomic Magnetic Moments (in μ_B) in the Ambient-Pressure hP9 and oP12 Phases of MnRhP with and without SOC

	hexagonal phase (hP9)							orthorhombic phase (oP12)						
	Mn		Rh		P			Mn		Rh		P		
	orbital	spin	orbital	spin	orbital	spin	total	orbital	spin	orbital	spin	orbital	spin	total
GGA		3.21		−0.03		−0.09	3.12		3.15		−0.01		−0.08	3.08
GGA + SO	0.01	3.20	0.00	−0.03	−0.00	−0.09	3.12	0.02	3.15	−0.00	−0.01	−0.00	−0.08	3.08

Table 2. Coordinates of Weyl Points for hP9 Phase in the BZ along with Their Respective Chiralities[a]

Weyl points	(k_x, k_y, k_z)	chirality
W_1^+	(0.279, −0.121, −0.213)	1
W_1^-	(−0.281, 0.116, −0.214)	−1
W_2^+	(0.280, 0.116, 0.213)	1
W_2^-	(−0.280, −0.123, 0.219)	−1
W_3^+	(−0.137, −0.226, 0.339)	1
W_3^-	(0.137, 0.226, 0.336)	−1
W_4^+	(−0.136, 0.226, −0.342)	1
W_4^-	(0.136, −0.226, −0.335)	−1
W_5^+	(0.316, −0.018, 0.249)	1
W_5^-	(−0.316, 0.013, 0.249)	−1
W_6^+	(0.315, 0.031, −0.259)	1
W_6^-	(−0.313, −0.020, −0.251)	−1

[a]$W_i^{\pm}$ represents the ith Weyl point with chirality ±1.

Table 3. Coordinates of Weyl Points for the oP12 Phase in the BZ along with Their Respective Chiralities[a]

Weyl points	(k_x, k_y, k_z)	chirality
W_1^+	(−0.202, 0.000, 0.000)	1
W_1^-	(0.202, 0.000, 0.000)	−1
W_2^+	(0.000, 0.035, −0.121)	1
W_2^-	(0.000, −0.040, 0.122)	−1

[a]$W_i^{\pm}$ represents the ith Weyl point with chirality ±1.

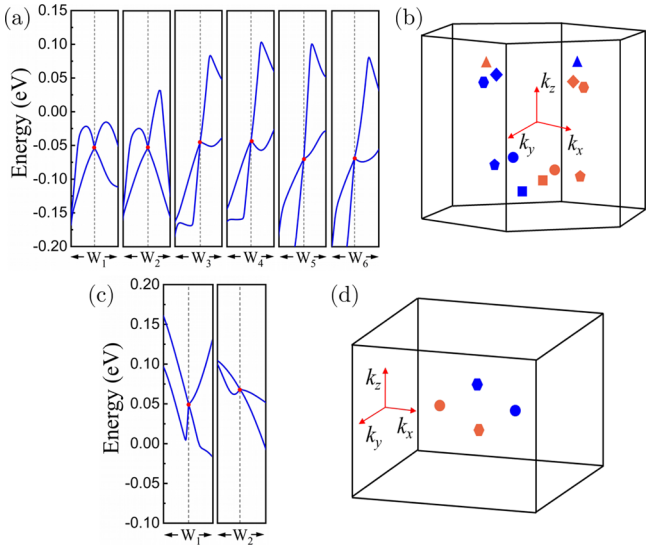

Figure 7. (a,b) Band dispersions around six positive chiral Weyl nodes along with the locus of 12 Weyl nodes in the bulk BZ of the hP9 phase. (c,d) 2D electronic band structures corresponding to Weyl nodes together with bulk BZ of the oP12 phase (orange: +ve and blue: −ve).

between $d_{x^2-y^2}$ and d_{xz} of "Mn" atoms. By introducing the SOC, these crossings are found to be gapped out. All these points lead toward the topological NL in the system in the $k_z = 0$ plane. A similar type of band crossing protected by mirror symmetry and band inversion along the Γ-M-K-Γ path in the $k_z = 0$ plane is also found in the hP9′ phase of MnRhP as shown in Figure S6c,d.

In order to confirm the presence of NLs in both high-pressure phases, we have continued with the (001) surface state calculations. Figure 8 gives the details of the (001) projected

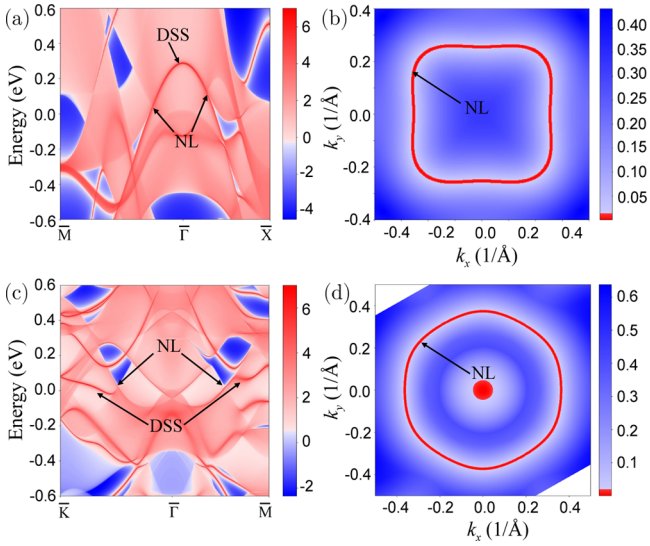

Figure 8. (a) Calculated (001) surface projected band structure of MnRhP in its tP6′ phase (at 15 GPa) highlighting the NL alongside with DSSs. (b) Corresponding energy gap plane. (c) (001) projected surface states of hP9′ phase (at 30 GPa) together with (d) energy gap plane, which show the NL in this phase.

surface state, which highlights the NL dispersion from the bulk bands and the emergent DSSs, along with the energy gap plane corresponding to the NL for both phases.

Being FM in nature, the tP6′ phase lacks the time-reversal symmetry and is expected to contain Weyl points in the presence of SOC. Similarly, due to the absence of the inversion symmetry, the hP9′ phase hosts the Weyl points with the inclusion of SOC. The magnetization along the [100] direction breaks the rotation C_{4z}, screw-axis rotation (S_{2y} and S_{2z}), and glide mirror symmetries (G_y and G_z) while preserving the inversion, glide mirror plane G_x, and screw-axis rotation S_{2x} symmetries in the tP6′ phase. In the case of hP9′, the inclusion of SOC splits the bands due to the lack of the inversion symmetry and generates Weyl points. With SOC, it preserves the horizontal mirror plane m_{001} and C_{3z}. For both phases, Weyl points with opposite chiralities are tabulated in Tables 4 and 5 and also marked in the BZ with the band dispersions near these Weyl nodes as shown in Figure 9. The presence of time-reversal symmetry in the hP9′ phase motivated us to determine the Z_2 invariants to check the weak or strong topology. The calculated values of Z_2 invariants are (1;001), making it a strong non-trivial topological material.

https://doi.org/10.1021/acs.jpcc.2c04603
J. Phys. Chem. C 2022, 126, 17328−17337

Table 4. Coordinates of Weyl Points for the tP6′ Phase at 15 GPa in the BZ along with Their Respective Chiralities[a]

Weyl points	(k_x, k_y, k_z)	chirality
W_1^+	(−0.229, −0.323, 0.160)	1
W_1^-	(0.229, −0.323, −0.159)	−1
W_2^+	(0.244, 0.583, 0.000)	1
W_2^-	(−0.243, 0.584, 0.000)	−1
W_3^+	(0.232, −0.592, 0.000)	1
W_3^-	(−0.232, −0.592, 0.000)	−1
W_4^+	(−0.226, 0.324, −0.159)	1
W_4^-	(0.226, 0.325, 0.159)	−1

[a]$W_i^{\pm}$ represents the ith Weyl point with chirality ±1.

Table 5. Coordinates of Weyl Points for the hP9′ Phase at 30 GPa in the BZ along with Their Respective Chiralities[a]

Weyl points	(k_x, k_y, k_z)	chirality
W_1^+	(−0.114, 0.312, −0.245)	1
W_1^-	(0.114, −0.312, −0.243)	−1
W_2^+	(−0.213, 0.252, 0.251)	1
W_2^-	(0.213, −0.252, 0.253)	−1
W_3^+	(0.325, −0.058, −0.252)	1
W_3^-	(−0.325, 0.058, −0.252)	−1
W_4^+	(−0.216, −0.249, −0.260)	1
W_4^-	(−0.217, −0.249, 0.256)	−1
W_5^+	(0.104, 0.312, −0.265)	1
W_5^-	(0.105, 0.312, 0.265)	−1
W_6^+	(−0.220, −0.239, 0.343)	1
W_6^-	(0.220, 0.239, 0.343)	−1

[a]$W_i^{\pm}$ represents the ith Weyl point with chirality ±1.

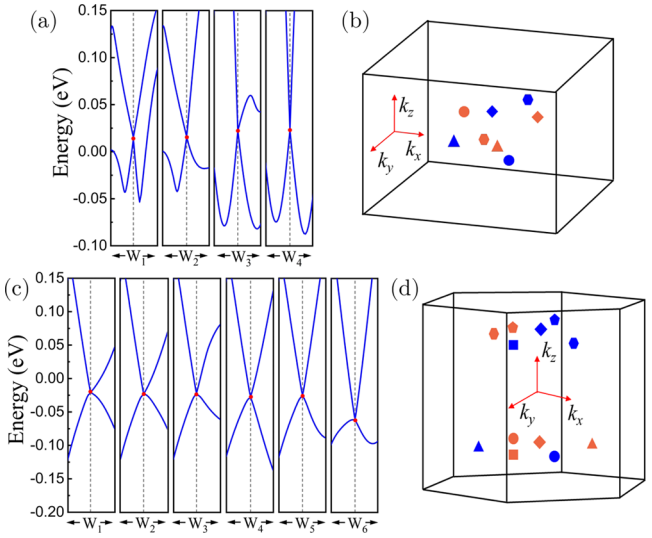

Figure 9. (a,b) Band dispersions around four positive chiral Weyl nodes in the tP6′ phase (at 15 GPa) along with the locus of Weyl nodes in the BZ of tP6′ phase. (c,d) 2D band dispersions corresponding to the Weyl points along with the positions of Weyl nodes in the BZ of the hP9′ phase (at 30 GPa) (orange: +ve and blue: −ve).

In addition, we have also applied the magnetization along the [001] direction. The calculated electronic properties are given in Figure S7. From Figure S7a, we observe in the case of the hP9 phase that the NL remains to be protected due to the presence of the m_{001} symmetry. Next to that, in the case of oP12 and tP6′ phases, the magnetization along the [001] direction preserves the inversion, screw-axis rotation S_{2z}, and glide mirror G_z symmetries but breaks the glide mirror symmetry (G_x and G_y) and screw-axis rotation symmetry (S_{2x} and S_{2y}), which might be the reason for opening the gaps in NL (see Figure S7b,c) and the generation of Weyl points.

TMs have been found to exhibit some unique properties like large anomalous Hall effect, anomalous Nernst effect, and so forth.[67,68] In Figure 10, we have provided the details of the

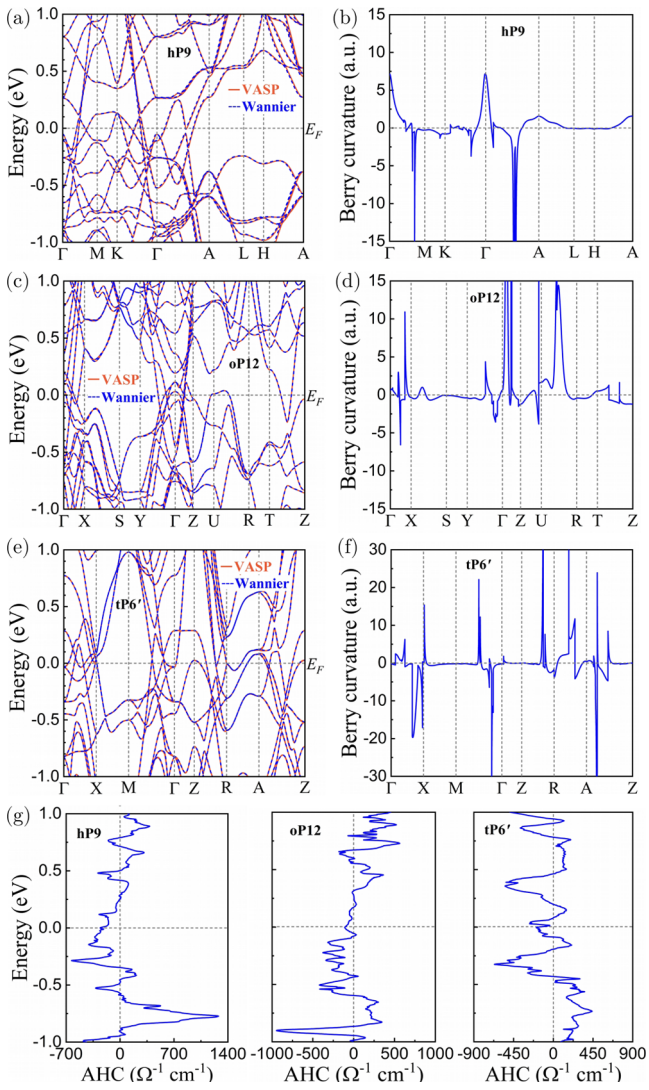

Figure 10. (a,c,e) Band structure of MnRhP with the inclusion of SOC (the band structures using VASP and WANNIER90 are shown in solid red and dashed blue lines, respectively). (b,d,f) Berry curvature along the high-symmetry path. (g) Anomalous Hall conductivity (AHC) for hP9, oP12, and tP6′ phases of MnRhP.

electronic band structure with SOC along with the WANNIER interpolated band structure, the Berry curvature ($\Omega_{yz}(k)$) along the high-symmetry band path, and the anomalous Hall conductivity (AHC) of hP9, oP12, and tP6′ phases of MnRhP. The AHC has been calculated from Berry curvature as follows[69,70]

$$\sigma_{yz} = \frac{-e^2}{\hbar}\int_{BZ}\frac{d^3k}{(2\pi)^3}\Omega_{yz}(k) \quad (1)$$

The inclusion of SOC opens up a gap at the crossing points, which is responsible for a non-vanishing Berry curvature. Hence,

https://doi.org/10.1021/acs.jpcc.2c04603
J. Phys. Chem. C 2022, 126, 17328−17337

we observe sharp peaks and valleys in the corresponding band path where the crossing points exist, as shown in Figure 10. We predict the magnitude of the AHC to be −257 Ω^{-1} cm^{-1} at the Fermi level, where we obtain the NL for the hP9 phase. The magnitude of the AHC increases to −630 Ω^{-1} cm^{-1} at the energy range of −0.29 eV and reaches a maximum value of 1282 Ω^{-1} cm^{-1} at an energy value of −0.77 eV. On the other hand, the obtained value of AHC for the oP12 phase is −106 Ω^{-1} cm^{-1} at the Fermi level and reaches the maximum (−944 Ω^{-1} cm^{-1}) at around −0.9 eV. The obtained value of the AHC for tP6′ is −165 Ω^{-1} cm^{-1} at the Fermi level, which reaches the maximum (−665 Ω^{-1} cm^{-1}) at −0.33 eV. Such large values of AHC are observed in other magnetic compounds like $MnPO_4$ (1265 Ω^{-1} cm^{-1})[71] and MnAlGe (700 Ω^{-1} cm^{-1}).[72]

CONCLUSIONS

In summary, we have performed a detailed ab initio study of the structural, electronic, magnetic, and topological properties of the intermetallic MnRhP compound. Our evolutionary structure searches and thermodynamic stability analysis provide insights into possible MnRhP polymorphs under different conditions. In particular, our proposed oP12 phase is a possible low-temperature ground state at ambient pressure. We identify three competing phases at high pressures, tP6′, hP9′, and oP12′, and illustrate that a powder XRD pattern simulated for hP9′ is in a reasonable agreement with the previously reported experimental data but explains only a subset of the observed peaks. An examination of the MnRhP phases for pressures up to 60 GPa and select MnMP phases across the 4d transition metal series helps establish the importance of the magnetic energy for the stability of Fe_2P-type materials. Our analysis of the intermetallic compound's electronic properties in the known (hP9) and proposed (oP12) ambient pressure structures uncovers the existence of an NL around the Γ-point with drumhead-like surface states. Evaluation of the magnetocrystalline anisotropy energy in the presence of SOC indicates that MnRhP prefers to stabilize in FM order with the [100] magnetization direction and that the NLs are gapped out to form six and two pairs of Weyl nodes for hP9 and oP12 phase, respectively. The non-triviality of this compound can be indirectly verified from the simulated large value of the anomalous Hall conductivity (1282 Ω^{-1} cm^{-1} for the hP9 phase and −944 Ω^{-1} cm^{-1} for the oP12 phase). The high-pressure tP6′ and hP9′ phases are also found to have interesting crossing points in the electronic structure along with the band inversion of Mn-d orbitals. The existence of signature topological features in the ambient- and high-pressure phases call for further investigation of this material.

ASSOCIATED CONTENT

Supporting Information

The Supporting Information is available free of charge at https://pubs.acs.org/doi/10.1021/acs.jpcc.2c04603.

Crystal structure information of hP9 phase at ambient pressure, hP9′ phase at 60 GPa pressure, oP12 phase at ambient pressure, oP12′ phase at 60 GPa pressure, tP6 phase at 20 GPa pressure, and tP6′ phase at 20 GPa pressure (ZIP)

Free energy corrections due to vibrational entropy in Fe_2P (Figure S19(a)); distribution of M−P bonds in two competing structures, hP9 and oP12, in MnRhP and Fe_2P (Figure S1(b)); phonon dispersion for hP9′ at 60 GPa (Figure S1(c)); volume dependencies on pressure for hP9 and hP9′ (Figure S1(d)); dynamical properties; comparison of MnRhP XRD patterns for hP9, oS18, hP9′, and oS18′ 60 GPa (Figure S2); phonon dispersion of hP9, oP12, tP6′, and hP9′ (Figure S3); magnetic properties; energies of different magnetic configurations in hP9 and oP12 (Table S1); FM and AFM configurations for hP9 and oP12 (Figure S4); the exchange coupling parameter and PDOS for hP9 and oP12 (Figure S5); electronic properties for tP6′ and hP9′ (Figure S6); electronic properties along [001] for hP9, oP12, and tP6′ (Figure S7); references (PDF)

AUTHOR INFORMATION

Corresponding Authors

G. Vaitheeswaran − *School of Physics, University of Hyderabad, Hyderabad 500046 Telangana, India;* orcid.org/0000-0002-2320-7667; Email: vaithee@uohyd.ac.in

V. Kanchana − *Department of Physics, Indian Institute of Technology Hyderabad, Medak 502 285 Telangana, India;* orcid.org/0000-0003-1575-9936; Email: kanchana@iith.ac.in

Authors

Jaspreet Singh − *Department of Physics, Indian Institute of Technology Hyderabad, Medak 502 285 Telangana, India*

Anuroopa Behatha − *Department of Physics, Indian Institute of Technology Hyderabad, Medak 502 285 Telangana, India*

Saba Kharabadze − *Department of Physics, Applied Physics and Astronomy, Binghamton University, State University of New York, Binghamton 13902-6000 New York, United States*

A. N. Kolmogorov − *Department of Physics, Applied Physics and Astronomy, Binghamton University, State University of New York, Binghamton 13902-6000 New York, United States*

Complete contact information is available at: https://pubs.acs.org/10.1021/acs.jpcc.2c04603

Notes

The authors declare no competing financial interest.

ACKNOWLEDGMENTS

Authors J.S., A.B., and V.K. acknowledge IIT Hyderabad and CDAC for computational facilities. S.K. and A.N.K. acknowledge the Extreme Science and Engineering Discovery Environment computational resources[73] (NSF award no. ACI-1548562, project no. TG-PHY190024). G.V. acknowledges the support from Institution of Eminence-University of Hyderabad through (UoH-IoE-RC3-21-046) for funding and CMSD, University of Hyderabad, for providing computational support. A.B. acknowledges DST-INSPIRE for fellowship. J.S. acknowledges CSIR for fellowship. V.K. acknowledges DST project with Grant number (CRG/2018/000220).

REFERENCES

(1) Ma, Y.; Eremets, M.; Oganov, A. R.; Xie, Y.; Trojan, I.; Medvedev, S.; Lyakhov, A. O.; Valle, M.; Prakapenka, V. Transparent dense sodium. *Nature* **2009**, *458*, 182−185.

(2) Drozdov, A. P.; Eremets, M. I.; Troyan, I. A.; Ksenofontov, V.; Shylin, S. I. Conventional superconductivity at 203 kelvin at high pressures in the sulfur hydride system. *Nature* **2015**, *525*, 73−76.

(3) Miao, M. Noble Gases in Solid Compounds Show a Rich Display of Chemistry With Enough Pressure. *Front. Chem.* **2020**, *8*, 962.

(4) Kolmogorov, A. N.; Shah, S.; Margine, E. R.; Kleppe, A. K.; Jephcoat, A. P. Pressure-Driven Evolution of the Covalent Network in CaB_6. *Phys. Rev. Lett.* **2012**, *109*, 075501.
(5) Oganov, A. R.; Lyakhov, A. O.; Valle, M. How Evolutionary Crystal Structure Prediction Works— and Why. *Acc. Chem. Res.* **2011**, *44*, 227−237.
(6) Wang, Y.; Lv, J.; Zhu, L.; Ma, Y. Crystal structure prediction via particle-swarm optimization. *Phys. Rev. B: Condens. Matter Mater. Phys.* **2010**, *82*, 094116.
(7) Pickard, C. J.; Needs, R. J. Ab initiorandom structure searching. *J. Phys.: Condens. Matter* **2011**, *23*, 053201.
(8) Amsler, M.; Goedecker, S. Crystal structure prediction using the minima hopping method. *J. Chem. Phys.* **2010**, *133*, 224104.
(9) Falls, Z.; Avery, P.; Wang, X.; Hilleke, K. P.; Zurek, E. The XtalOpt Evolutionary Algorithm for Crystal Structure Prediction. *J. Phys. Chem. C* **2021**, *125*, 1601−1620.
(10) Hajinazar, S.; Thorn, A.; Sandoval, E. D.; Kharabadze, S.; Kolmogorov, A. N. MAISE: Construction of neural network interatomic models and evolutionary structure optimization. *Comput. Phys. Commun.* **2021**, *259*, 107679.
(11) Duan, D.; Liu, Y.; Tian, F.; Li, D.; Huang, X.; Zhao, Z.; Yu, H.; Liu, B.; Tian, W.; Cui, T. Pressure-induced metallization of dense $((H_2S)_2H_2)$ with high-T_C superconductivity. *Sci. Rep.* **2014**, *4*, 6968.
(12) Kolmogorov, A. N.; Shah, S.; Margine, E. R.; Bialon, A. F.; Hammerschmidt, T.; Drautz, R. New Superconducting and Semiconducting Fe-B Compounds Predicted with an Ab Initio Evolutionary Search. *Phys. Rev. Lett.* **2010**, *105*, 217003.
(13) Gou, H.; Dubrovinskaia, N.; Bykova, E.; Tsirlin, A. A.; Kasinathan, D.; Schnelle, W.; Richter, A.; Merlini, M.; Hanfland, M.; Abakumov, A. M.; et al. Discovery of a Superhard Iron Tetraboride Superconductor. *Phys. Rev. Lett.* **2013**, *111*, 157002.
(14) Kolmogorov, A. N.; Curtarolo, S. Theoretical study of metal borides stability. *Phys. Rev. B: Condens. Matter Mater. Phys.* **2006**, *74*, 224507.
(15) Kolmogorov, A. N.; Hajinazar, S.; Angyal, C.; Kuznetsov, V. L.; Jephcoat, A. P. Synthesis of a predicted layered LiB via cold compression. *Phys. Rev. B: Condens. Matter Mater. Phys.* **2015**, *92*, 144110.
(16) Chiu, C. K.; Teo, J. C. Y.; Schnyder, A. P.; Ryu, S. Classification of topological quantum matter with symmetries. *Rev. Mod. Phys.* **2016**, *88*, 035005.
(17) Yang, S. A. Dirac and Weyl Materials: Fundamental Aspects and Some Spintronics Applications. *SPIN* **2016**, *06*, 1640003.
(18) Bansil, A.; Lin, H.; Das, T. Colloquium: Topological band theory. *Rev. Mod. Phys.* **2016**, *88*, 021004.
(19) Dai, X. Weyl fermions go into orbit. *Nat. Phys.* **2016**, *12*, 727−728.
(20) He, T.; Zhang, X.; Meng, W.; Jin, L.; Dai, X.; Liu, G. Topological nodal lines and nodal points in the antiferromagnetic material β-Fe_2PO_5. *J. Mater. Chem. C* **2019**, *7*, 12657−12663.
(21) Weng, H.; Fang, C.; Fang, Z.; Dai, X. Topological semimetals with triply degenerate nodal points in θ-phase tantalum nitride. *Phys. Rev. B* **2016**, *93*, 241202.
(22) Ahn, K. H.; Pickett, W. E.; Lee, K. W. Coexistence of triple nodal points, nodal links, and unusual flat bands in intermetallic APd_3 (A=Pb, Sn). *Phys. Rev. B* **2018**, *98*, 035130.
(23) Fu, B. B.; Yi, C. J.; Zhang, T. T.; Caputo, M.; Ma, J. Z.; Gao, X.; Lv, B. Q.; Kong, L. Y.; Huang, Y. B.; Richard, P.; et al. Dirac nodal surfaces and nodal lines in ZrSiS. *Sci. Adv.* **2019**, *5*, No. eaau6459.
(24) Fang, C.; Weng, H.; Dai, X.; Fang, Z. Topological nodal line semimetals. *Chin. Phys. B* **2016**, *25*, 117106.
(25) Burkov, A. A.; Hook, M. D.; Balents, L. Topological nodal semimetals. *Phys. Rev. B: Condens. Matter Mater. Phys.* **2011**, *84*, 235126.
(26) Fang, C.; Weng, H.; Dai, X.; Fang, Z. Topological nodal line semimetals. *Chin. Phys. B* **2016**, *25*, 117106.
(27) Xu, G.; Weng, H.; Wang, Z.; Dai, X.; Fang, Z. Chern Semimetal and the Quantized Anomalous Hall Effect in $HgCr_2Se_4$. *Phys. Rev. Lett.* **2011**, *107*, 186806.
(28) Cuamba, A. S.; Lu, H. Y.; Hao, L.; Ting, C. S.Electronic structure and nontrivial topological surface states in ZrRuP and ScPd3 compounds. **2018**, arXiv:1801.01113.
(29) Qian, Y.; Nie, S.; Yi, C.; Kong, L.; Fang, C.; Qian, T.; Ding, H.; Shi, Y.; Wang, Z.; Weng, H.; et al. Topological electronic states in HfRuP family superconductors. *npj Comput. Mater.* **2019**, *5*, 121.
(30) Yamakage, A.; Yamakawa, Y.; Tanaka, Y.; Okamoto, Y. Line-Node Dirac Semimetal and Topological Insulating Phase in Noncentrosymmetric Pnictides CaAgX (X=P, As). *J. Phys. Soc. Jpn.* **2016**, *85*, 013708.
(31) Beckman, O.; Lundgren, L.Compounds of transition elements with non-metals; *Handbook of Magnetic Materials*; Elsevier, 1991; Vol. *6*, Chapter 3; pp 181−287.
(32) Kanomata, T.; Kawashima, T.; Utsugi, H.; Goto, T.; Hasegawa, H.; Kaneko, T. Magnetic properties of the intermetallic compounds MM′X (M=Cr,Mn, M′=Ru,Rh,Pd, and X=P,As). *J. Appl. Phys.* **1991**, *69*, 4639−4641.
(33) Ohta, S.; Kanomata, T.; Kaneko, T. Magnetic properties of CrRhAs and CrRuAs. *J. Magn. Magn. Mater.* **1990**, *90−91*, 171−172.
(34) Harada, T.; Kanomata, T.; Kaneko, T. Transport and magnetic properties of the intermetallic compounds MnRuAs and MnPdAs. *J. Magn. Magn. Mater.* **1990**, *90−91*, 169−170.
(35) Kadomatsu, H.; Isoda, M.; Tohma, K.; Fujii, H.; Okamoto, T.; Fujiwara, H. Pressure-Induced Antiferromagnetism of Fe_2P. *J. Phys. Soc. Jpn.* **1985**, *54*, 2690−2699.
(36) Fujii, N.; Zach, R.; Ishizuka, M.; Ono, F.; Kanomata, T.; Endo, S. Pressure-induced magnetic transition in MnRhAs. *J. Magn. Magn. Mater.* **2001**, *224*, 12−16.
(37) Eto, T.; Yamagishi, M.; Ishizuka, M.; Endo, S.; Ashida, T.; Kanomata, T.; Kikegawa, T.; Zach, R. Pressure-induced structural transition in intermetallic compounds MnRhP and MnRhAs. *J. Alloys Compd.* **2000**, *307*, 96−100.
(38) Sereika, R.; Wu, W.; Park, C.; Kenney-Benson, C.; Brewe, D. L.; Heald, S. M.; Zhang, J.; Yesudhas, S.; Deng, H.; Chen, B.; et al. Prolonged mixed phase induced by high pressure in MnRuP. *Phys. Rev. B* **2018**, *97*, 214103.
(39) Kanomata, T.; Kawashima, T.; Yoshida, H.; Kaneko, T. Pressure effect on the Curie temperatures of MnRuAs, MnPdAs and MnRhP. *AIP Conf. Proc.* **1994**, *309*, 1469−1472.
(40) Kanomata, T.; Shirakawa, K.; Yasui, H.; Kaneko, T. Effect of hydrostatic pressure on the magnetic transition temperatures of MnRhAs. *J. Magn. Magn. Mater.* **1987**, *68*, 286−290.
(41) Kaneko, T.; Kanomata, T.; Kawashima, T.; Mori, S.; Miura, S.; Nakagawa, Y. High-field magnetization in intermetallic compounds MM′X (M=Mn, Cr; M′=Ru, Rh, Pd; X=As, P). *Phys. B* **1992**, *177*, 123−126.
(42) Sato, K.; Suzuki, N.; Kanomata, T.; Yamauchi, H.; Yoshida, H.; Kaneko, T.; Yamaguchi, Y.; Kamishima, T.; Goto, T. Pressure dependence of the Curie temperature and spontaneous magnetization of MnRhP. *J. Magn. Magn. Mater.* **1998**, *177−181*, 1381−1382.
(43) Kresse, G.; Hafner, J. Ab initio molecular dynamics for liquid metals. *Phys. Rev. B: Condens. Matter Mater. Phys.* **1993**, *47*, 558−561.
(44) Kresse, G.; Furthmüller, J. Efficiency of ab-initio total energy calculations for metals and semiconductors using a plane-wave basis set. *Comput. Mater. Sci.* **1996**, *6*, 15−50.
(45) Kresse, G.; Joubert, D. From ultrasoft pseudopotentials to the projector augmented-wave method. *Phys. Rev. B: Condens. Matter Mater. Phys.* **1999**, *59*, 1758−1775.
(46) Perdew, J. P.; Burke, K.; Ernzerhof, M. Generalized Gradient Approximation Made Simple. *Phys. Rev. Lett.* **1996**, *77*, 3865−3868.
(47) Ceperley, D. M.; Alder, B. J. Ground State of the Electron Gas by a Stochastic Method. *Phys. Rev. Lett.* **1980**, *45*, 566−569.
(48) Perdew, J. P.; Zunger, A. Self-interaction correction to density-functional approximations for many-electron systems. *Phys. Rev. B: Condens. Matter Mater. Phys.* **1981**, *23*, 5048−5079.
(49) Klimeš, J.; Bowler, D. R.; Michaelides, A. Chemical accuracy for the van der Waals density functional. *J. Phys.: Condens. Matter* **2009**, *22*, 022201.

https://doi.org/10.1021/acs.jpcc.2c04603
J. Phys. Chem. C 2022, 126, 17328−17337

(50) Sun, J.; Ruzsinszky, A.; Perdew, J. P. Strongly Constrained and Appropriately Normed Semilocal Density Functional. *Phys. Rev. Lett.* **2015**, *115*, 036402.
(51) Monkhorst, H. J.; Pack, J. D. Special points for Brillouin-zone integrations. *Phys. Rev. B: Solid State* **1976**, *13*, 5188−5192.
(52) Ebert, H.; Ködderitzsch, D.; Minár, J. Calculating condensed matter properties using the KKR-Green's function method-recent developments and applications. *Rep. Prog. Phys.* **2011**, *74*, 096501.
(53) Gonze, X.; Lee, C. Dynamical matrices, Born effective charges, dielectric permittivity tensors, and interatomic force constants from density-functional perturbation theory. *Phys. Rev. B: Condens. Matter Mater. Phys.* **1997**, *55*, 10355−10368.
(54) Mostofi, A. A.; Yates, J. R.; Pizzi, G.; Lee, Y. S.; Souza, I.; Vanderbilt, D.; Marzari, N. An updated version of wannier90: A tool for obtaining maximally-localised Wannier functions. *Comput. Phys. Commun.* **2014**, *185*, 2309−2310.
(55) Wu, Q.; Zhang, S.; Song, H. F.; Troyer, M.; Soluyanov, A. A. WannierTools: An open-source software package for novel topological materials. *Comput. Phys. Commun.* **2018**, *224*, 405−416.
(56) Bhat, S. S.; Gupta, K.; Bhattacharjee, S.; Lee, S. C. Role of zero-point effects in stabilizing the ground state structure of bulk Fe_2P. *J. Phys.: Condens. Matter* **2018**, *30*, 215401.
(57) Larson, P.; Mazin, I. I.; Singh, D. J. Magnetism, critical fluctuations, and susceptibility renormalization in Pd. *Phys. Rev. B: Condens. Matter Mater. Phys.* **2004**, *69*, 064429.
(58) Scheerlinck, D.; Legrand, E. Neutron diffraction study of the magnetic structure of Fe_2P. *Solid State Commun.* **1978**, *25*, 181−184.
(59) Daeumer, M.; Sandoval, E. D.; Azizi, A.; Bagheri, M. H.; Bae, I.-T.; Panta, S.; Koulakova, E. A.; Cotts, E.; Arvin, C. L.; Kolmogorov, A. N.; et al. Orientation-dependent transport properties of Cu_3Sn. *Acta Mater.* **2022**, *227*, 117671.
(60) Kafle, G. P.; Heil, C.; Paudyal, H.; Margine, E. R. Electronic, vibrational, and electron-phonon coupling properties in $SnSe_2$ and SnS_2 under pressure. *J. Mater. Chem. C* **2020**, *8*, 16404−16417.
(61) Fabbris, G.; Thorn, A.; Bi, W.; Abramchuk, M.; Bahrami, F.; Kim, J. H.; Shinmei, T.; Irifune, T.; Tafti, F.; Kolmogorov, A. N.; et al. Complex pressure-temperature structural phase diagram of the honeycomb iridate Cu_2IrO_3. *Phys. Rev. B* **2021**, *104*, 014102.
(62) Klotz, S.; Chervin, J. C.; Munsch, P.; Le Marchand, G. Hydrostatic limits of 11 pressure transmitting media. *J. Phys. D: Appl. Phys.* **2009**, *42*, 075413.
(63) Errandonea, D.; Meng, Y.; Somayazulu, M.; Häusermann, D. Pressure-induced $\alpha \rightarrow \omega$ transition in titanium metal: a systematic study of the effects of uniaxial stress. *Phys. B* **2005**, *355*, 116−125.
(64) Wang, P.; He, D.; Xu, C.; Ren, X.; Lei, L.; Wang, S.; Peng, F.; Yan, X.; Liu, D.; Wang, Q.; et al. High-pressure x-ray diffraction study of YBO_3/Eu^{3+}, $GdBO_3$, and $EuBO_3$: Pressure-induced amorphization in $GdBO_3$. *J. Appl. Phys.* **2014**, *115*, 043507.
(65) Garg, A. B.; Errandonea, D.; Rodríguez-Hernández, P.; Muñoz, A. $ScVO_4$ under non-hydrostatic compression: a new metastable polymorph. *J. Phys.: Condens. Matter* **2016**, *29*, 055401.
(66) Sun, J.-P.; Zhang, D.; Chang, K. Coexistence of topological nodal lines, Weyl points, and triply degenerate points in TaS. *Phys. Rev. B* **2017**, *96*, 045121.
(67) Manna, K.; Sun, Y.; Muechler, L.; Kübler, J.; Felser, C. Heusler, Weyl and Berry. *Nat. Rev. Mater.* **2018**, *3*, 244−256.
(68) Noky, J.; Zhang, Y.; Gooth, J.; Felser, C.; Sun, Y. Giant anomalous Hall and Nernst effect in magnetic cubic Heusler compounds. *npj Comput. Mater.* **2020**, *6*, 77.
(69) Xiao, D.; Chang, M. C.; Niu, Q. Berry phase effects on electronic properties. *Rev. Mod. Phys.* **2010**, *82*, 1959−2007.
(70) Nagaosa, N.; Sinova, J.; Onoda, S.; MacDonald, A. H.; Ong, N. P. Anomalous Hall effect. *Rev. Mod. Phys.* **2010**, *82*, 1539−1592.
(71) Hsu, C. H.; Sreeparvathy, P. C.; Barman, C. K.; Chuang, F. C.; Alam, A. Coexistence of topological nontrivial and spin-gapless semiconducting behavior in $MnPO_4$: A composite quantum compound. *Phys. Rev. B* **2021**, *103*, 195143.
(72) Guin, S. N.; Xu, Q.; Kumar, N.; Kung, H. H.; Dufresne, S.; Le, C.; Vir, P.; Michiardi, M.; Pedersen, T.; Gorovikov, S.; et al. 2D-Berry-Curvature-Driven Large Anomalous Hall Effect in Layered Topological Nodal-Line MnAlGe. *Adv. Mater.* **2021**, *33*, 2006301.
(73) Towns, J.; Cockerill, T.; Dahan, M.; Foster, I.; Gaither, K.; Grimshaw, A.; Hazlewood, V.; Lathrop, S.; Lifka, D.; Peterson, G. D.; et al. XSEDE: Accelerating Scientific Discovery. *Comput. Sci. Eng.* **2014**, *16*, 62−74.

https://doi.org/10.1021/acs.jpcc.2c04603
J. Phys. Chem. C 2022, 126, 17328−17337